IET Control Theory & Applications

Research Article

IET Journals
The Institution of Engineering and Technology

Sideslip angle estimation of ground vehicles: a comparative study

ISSN 1751-8644
Received on 25th April 2020
Revised 14th October 2020
Accepted on 25th November 2020
E-First on 12th March 2021
doi: 10.1049/iet-cta.2020.0516
www.ietdl.org

Jizheng Liu[1], Zhenpo Wang[1], Lei Zhang[1] ✉, Paul Walker[2]

[1]*National Engineering Laboratory for Electric Vehicles, Beijing Institute of Technology, 5 South Zhongguancun Street, Beijing 100081, People's Republic of China*

[2]*Faculty of Engineering and Information Technology, University of Technology Sydney, Ultimo, NSW 2007, Australia*

✉ *E-mail: Lei_zhang@bit.edu.cn*

Abstract: Vehicle sideslip angle is a major indicator of dynamics stability for ground vehicles; but it is immeasurable with commercially-available sensors. Sideslip angle estimation has been the focus of intensive research in past decades, resulting in a rich library of related literature. This study presents a comprehensive evaluation of state-of-the-art sideslip angle estimation methods, with the primary goal of quantitatively revealing their strengths and limitations. These include kinematics-, dynamics- and neural network-based estimators. A hardware-in-loop system is purposely established to examine their performance under four typical manoeuvres. The results show that the dynamics-based estimators are suitable at low vehicle velocities when tires operate in the linear region. In contrast, the kinematics-based methods yield superior estimation performance at high vehicle velocities, and the inclusion of the dual GPS receivers is beneficial even when there is large disturbance to the steering angle. Of utmost importance, it is experimentally manifested that the neural network-based estimator can perform well in all manoeuvres once the training datasets are properly selected.

1 Introduction

In order to improve vehicle safety and reduce road accident casualties, active control systems (ACSs) have been rapidly developed and increasingly adopted in mass production vehicles [1, 2]. These ACSs mainly include the active steering system (ASS) [3, 4], electronic stability controller (ESC) [5], direct yaw moment control [6], acceleration slip regulation [7] and the like. They can be utilised independently or in combination to enhance handling performance and stability of vehicles. Large-scale applications of ACSs are foreseeable with the development of automotive electrification and autonomous driving technology [8–10]. A prerequisite for efficient functionalities of these ACSs is accurate and real-time acquisition of vehicle sideslip angle that is indicative of vehicle dynamics stability [11, 12]. It can also be used as a control variable [13, 14]. However, it is commercially prohibitive to obtain the sideslip angle via direct measurements such as using high-precision optical sensors and combined inertial navigators. This necessitates the development of enabling estimation schemes based on conventional sensor suites.

Vehicle sideslip angle is strongly related to kinematic and dynamic responses of vehicles. It is expressed as the arc-tan function of the ratio of the lateral over the longitudinal vehicle velocity [11]. Longitudinal vehicle velocity can be obtained from global position system (GPS) signal or from integrating wheel rotational speed; but direct acquisition of the lateral velocity from the GPS signal is unattainable due to low signal-to-noise ratio (SNR) [15].

A rich library of previous works on sideslip angle estimation has been presented in the literature, which can be classified into two categories, i.e. model- and neural network (NN)-based methods. For the former [16], both kinematics and dynamics models can be used to describe the relationship between vehicle sideslip angle and other vehicle parameters and/or states [17]. The key difference lies in that tire forces are usually accounted for in dynamics models so that yaw and lateral motions can be linked in the sideslip angle description [18]. The performance of model-based the sideslip angle estimators is subject to vehicle modelling accuracy and sensoring capability. However, the non-linearity of the used vehicle models and their complex coupling effects with ever-varying driving conditions render it challenging to obtain satisfying estimation performance.

NN models can be utilised to delineate vehicle dynamics with no need of knowing intrinsic vehicle parameters. With an appropriate model structure and rich and diverse training datasets, NN-based methods show great potential for sideslip angle estimation as indicated in some preliminary studies [19]. Apart from direct sideslip angle estimation, the estimated results can also serve as a pseudo-estimate that is reckoned as a priori of an integrated model-based estimator [20]. This is termed as pseudo multi-sensor fusion. However, the requirements for the quality and quantity of the training data significantly limit their applicability. On one hand, oversized training datasets and complicated model structure mean high computational burden, which makes it infeasible for real-time implementation in embedded controllers [16]. On the other hand, the scarcity of competent training datasets that can inclusively represent comprehensive driving scenarios may lead to the under-fitting problem. In recent years, with the rapid development of intelligent transportation systems (ITSs) and vehicle-to-vehicle and vehicle-to-infrastructure techniques can provide additional information for enhancing sideslip angle estimation performance [21–23].

There are already several review papers available in the literature, covering multi-faceted research on vehicle sideslip angle estimation [16, 24–27]. However, there is lack of study to systematically examine the performance of state-of-the-art estimation methods in a quantitative manner. Besides, a detailed analysis on the advantages and limitations of each method based on comprehensive experimentation is also absent.

In order to bridge the mentioned gap, this study presents a comprehensive evaluation of the exiting vehicle sideslip angle estimation methods including kinematics-, dynamics- and NN-based estimators. Their respective characteristics are summarised and analysed based on comprehensive hardware-in-loop (HIL) experimentation. In particular, specific application scopes for each method are provided.

The remainder of the paper is arranged as follows. Section 2 gives an overview of the commonly used sideslip angle estimation methods. Section 3 elaborates on the detailed formulations of each

method. Section 4 presents simulation results and gives in-depth analysis, followed by the key conclusions summarised in Section 5.

2 Overview of sideslip angle estimation methods

Vehicle sideslip angle is calculated based on the accurate knowledge of the longitudinal and lateral vehicle velocities. It can be expressed with different formulations such as

$$\beta = \arctan\left(\frac{v_y}{v_x}\right) \tag{1}$$

$$\beta = \nu - \psi \tag{2}$$

$$\beta = \begin{cases} \alpha_f + \delta_f - \dfrac{a\omega_z}{v_x} \\ \alpha_r + \dfrac{b\omega_z}{v_x} \end{cases} \tag{3}$$

where β is the vehicle sideslip angle, v_x and v_y are the longitudinal and the lateral vehicle velocity, ν and ψ are the heading angle and the yaw angle of the vehicle, α_f and α_r are the sideslip angles of the front and rear tires, δ_f is the steering angle of the front wheels, ω_z is the yaw rate of the vehicle, and a and b are the distances between the centre of gravity (CG) to the front and the rear axle, respectively.

For the expression in (1), the longitudinal vehicle velocity can be readily inferred based on the rotational speed and effective radius of wheels [28], which makes it a core to precisely acquire the lateral velocity. As for (2), the vehicle heading angle is available in GPS signal, and the yaw angle can be derived by the yaw rate integration. In (3), the steering angle of the front wheels and the longitudinal velocity and yaw rate of the vehicle are all measurable while the sideslip angles of the front and rear wheels are determined by the lateral tire force and tire properties. Apart from the above-mentioned expressions, sideslip angle is also subject to other vehicle states such as lateral accelerations and roll rate. The complex relationship between sideslip angle and other vehicle parameters and/or states makes it extremely difficult to achieve sideslip angle estimation in real time.

2.1 Kinematics-based methods

Kinematics-based methods mainly concern with kinematic vehicle states including velocities and accelerations. In this aspect, Chen and Hsieh [17] proposed a 2-DOF kinematic model considering wheel speeds and measurable signals from an inertial measurement unit (IMU) such as longitudinal and lateral accelerations and yaw rate of the vehicle. Kim and Ryu [29] utilised a similar method by incorporating the longitudinal velocity variation. Farrelly and Wellstead [30] further improved the convergence performance of the lateral velocity estimator by combining the state and observation equations. The high-precision sensors for vehicle motion measurement can provide additional information to elevate estimation performance. For instance, Madhusudhanan *et al.* extended the vehicle model with pitch and roll motions [31, 32]. In order to cope with sensor noises, Selmanaj *et al.* [33, 34] employed a heuristic scheduling method to improve the robustness of a kinematics-based estimator.

With the development of the global navigation satellite system, GPS has been widely used in mass production vehicles [35]. On top of this, Bevly *et al.* [36] proposed a lateral velocity estimation method by combining a GPS with an IMU. They further included the heading angle from the GPS and the yaw angle from the IMU for better estimation effect [37]. Guo *et al.* [38] extended system state space with the biases from measured lateral and longitudinal accelerations in order to improve robustness.

Apart from GPS, the magnetometer is another sensor that can be utilised for sideslip angle estimation. In [39, 40], Yoon *et al.* estimated yaw and roll angles by combining angular rates and magnetic field measurements for longitudinal and lateral velocity estimations.

However, sideslip angle estimation schemes based on GPS are usually compromised by the low update rate problem. To solve this problem, Yoon and Peng employed GPS with dual receivers to increase the update rate [41]. The receivers are installed so that the yaw angle rate and longitudinal and lateral velocities can be directly derived. An extended Kalman filter (EKF) is employed to modify the derivations with measurements from an IMU. Benefiting from the wide application of GPS, the combination of GPS and IMU shows great potential for improving the accuracy of sideslip angle estimation [42].

2.2 Dynamics-based methods

The major characteristic of dynamics-based methods is the involvement of the longitudinal and lateral tire forces. There are a variety of tire models available to describe tire forces, each with their own strengths and limitations. A plethora of observers can be used and an appropriate combination of a tire model and an enabling observer holds the key to accurate sideslip angle estimation. The commonly used observers include EKF [18, 42–58], unscented Kalman filter (UKF) [50, 55, 59–64], sliding mode observer (SMO) [42, 44, 45, 65, 66] and the forth [67–79]. In order to further improve estimation accuracy, the underlying vehicle parameters are simultaneously estimated in some studies.

Vehicle dynamic models combined with linear tire models are widely utilised. For instance, Fukada [80] proposed a transfer function to describe the relationship between sideslip angle and other vehicle states using a linear tire model. Stéphant *et al.* [42, 45, 65] compared the difference between the linear and nonlinear vehicle models, and the impact of modelling accuracy on sideslip angle estimation was underscored. Nevertheless, the linear tire model has limited accuracy especially when tires enter into the non-linear region. Some studies focused on improving observer design. For example, Cheli *et al.* integrated a kinematic-integral estimator and a dynamics-based observer based on fuzzy logic [81]. Similarly, Bechtoff *et al.* used the EKF to estimate sideslip angle based on conventional ESC sensors without heuristics [53]. Strano *et al.* testified that the state-dependent-Riccati-equation filter could be a valid selection as the knowledge of intrinsic parameters is not required [77]. Chen *et al.* verified several observers on an in-wheel-motor-drive electric vehicle (IWMD EV) since the longitudinal force and velocity at each wheel can be accurately acquired [56, 74, 75].

The above-mentioned studies invariably considered the lateral tire force as a linear function of tire slip angle, which is given by

$$\begin{aligned} F_{fy} &= C_f \alpha_f \\ F_{ry} &= C_r \alpha_r \end{aligned} \tag{4}$$

where F_{fy} and F_{ry} are the lateral forces of the front and rear tires, and C_f and C_r are the cornering stiffnesses of the front and rear tires. However, the linear model is inaccurate when the slip angle becomes large.

In order to improve the accuracy of vehicle dynamics models, some adaptive algorithms such as the recursive least square (RLS) were adopted to online estimate vehicle parameters such as cornering stiffness [44, 50, 52, 54, 57, 82]. In this aspect, linear tire models with norm-bounded uncertainty were employed in [72, 73, 83]. The uncertain parameters were validated through experimental tests, which endows the linear tire model with higher reliability. In [43, 48, 59, 60, 68, 70, 71], the Dugoff tire model was employed to explicitly express the lateral and longitudinal tire forces as the functions of the tire slip angle, slip ratio, vertical load and tire–road friction coefficient. Like the Dugoff tire model, the Magic formula was also popularly employed as indicated in [47, 49, 51, 58, 61–63, 76, 84], which derives the lateral and longitudinal tire forces as the functions of several tire states.

With the development of sensoring technology, tire forces can be directly measured. For instance, Madhusudhanan *et al.* and Nam *et al.* used a load bearing sensor and the MSHub units to obtain tire forces, respectively [12, 44, 85, 86]. However, the measured lateral and longitudinal tire forces are not suitable for sideslip angle estimation in mass production vehicles since these sensors are

commercially prohibited and also highly susceptible to road adhesion coefficient variation.

With respect to observer design, Madhusudhanan *et al.* utilised the linear KF based on measured lateral forces [85, 86] for side slip angle estimation. For non-linear dynamics models, the EKF is the most widely utilised observer [18, 42–45, 47–54, 56–58]. However, due to the first-order approximation inherent with the Jacobian matrix calculation, the linearisation error persistently exists in the EKF. Instead, the UKF can use the UT transform to avoid linearisation [48, 55, 59–64], and shows higher accuracy. Apart from the KF-based observers, other non-linear observers are also applied. For instance, Chen *et al.* discussed the relationship between the orders of the employed vehicle model, and proposed a full-order SMO [66]. Zhang *et al.* established an energy-to-peak filter which formulates the relationship between sideslip angle and measured yaw rate [72]. Ding *et al.* employed a Luenberger observer with tuned parameters in specific manoeuvres [68]. Gao *et al.* proposed a high gain observer based on input–output linearisation, which exhibits higher accuracy than the EKF [69]. Chen *et al.* proposed an online gradient descent algorithm which can suppress the influence of sensor noises, longitudinal velocity variation and tire force non-linearity [76].

Sideslip angle can be estimated in combination with numerous road states through co-estimation schemes. In [57, 70, 82], road bank angle is estimated in combination with sideslip angle, which can improve the stability of observers in extreme manoeuvres. Similarly, road friction coefficient can also be online replenished to better describe the tire–road interactive forces [47, 67–69, 76, 87].

2.3 NN-based method

The efficacy of the existing model-based estimation methods is strongly sensitive to model parameters and is only verified under a limited range of driving conditions. Moderate model parameter deviations may render them diverge in complex and ever-varying driving conditions. To meet this challenge, NN-based methods represent a promising solution. With the development of decentralised control in vehicle-to-everything and the improvement of on-board controllers in processing capability [22], the feasibility of NNs for vehicle state estimation and control becomes possible. Generally, NNs have the ability to emulate the complex relationship between the inputs and outputs, and are also robust to measurement drift and noises [16].

Various NN models have been presented for vehicle sideslip angle estimation in the literature. For example, Kato *et al.* first applied a NN model in combination with a kinematics-based estimator for sideslip angle estimation [88]. In order to improve estimation accuracy, Hideaki *et al.* further considered the input data in past time steps, and proposed a time-delay NN [89]. Analogously, Du *et al.* used a back-propagation NN to predict sideslip angle [90]. The results show that the NN-based estimation algorithm can yield good performance at high vehicle velocities. Similarly, Chindamo *et al.* put forward a succinct approach to obtain the training datasets for NN model training in specific manoeuvres [91]. Torben Gräber *et al.* [92] presented a supervised machine learning scheme that consists of a recurrent NN with gated recurrent units, an additional input projection and a regression head. The results show that the presented method exhibits excellent estimation performance with good generalisation over different tires, road surfaces and driving conditions. Miao *et al.* presented a novel sideslip angle soft-sensor using the NN left inversion to estimate sideslip angle for an IWMD EV [93]. Besides, different variants of modified NNs are also used to improve the performance of sideslip angle estimation. For example, Melzi *et al.* employed the feedback NN with time-delay modules [19, 94].

The NN-based method is based on the signals measured by onboard sensors. To improve estimation robustness, data preprocessing or vehicle state identification is considered. In this regard, Martino *et al.* employed the principle component analysis (PCA) to reduce the number of dimensions of raw training data [95]. Bonfitto *et al.* [96] presented a NN-based algorithm in tandem with road condition identification.

Except for the above-mentioned methods, the post-processing of the estimation results can also contribute to estimation performance improvement. Boada *et al.* used an integrated method consisting of the adaptive neuro-fuzzy inference system (ANFIS) and the UKF to estimate sideslip angle [97, 98]. The output of the ANFIS is regarded as a pseudo-estimate, and the UKF-based dynamic model is employed as a noise filter to minimise the mean square error of the estimate. Novi *et al.* [99] proposed a similar method, which combines a NN with an UKF observer.

3 Sideslip angle estimation methods

In this section, several sideslip angle estimation methods are presented in greater details.

3.1 Kinematics-based methods

Two kinematics-based methods are introduced and compared, and they are the GPS-IMU fusion and the DPGS-IMU fusion.

3.1.1 GPS-IMU fusion: The heading angle of the vehicle is available in the GPS signal, and the yaw angle can be derived by integrating the measured yaw rate from the IMU as shown in (5). The sideslip angle can thus be calculated as shown in (6). However, the direct integration can be biased by the measurement noises, which necessitates the preprocessing of the GPS and IMU signals. A kinematic model is illustrated in Fig. 1, in which N means the direction of the North in the earth coordinate and v_G is the vehicle velocity provided by the GPS signal.

$$\psi = \int \omega_z \tag{5}$$

$$\beta_{\text{int}} = \nu + \psi \tag{6}$$

Based on the sideslip angle obtained based on direct integration, the lateral and longitudinal velocities v_x and v_y in the vehicle coordinate can be obtained by

$$\begin{aligned} v_x &= v_G \cos \beta_{\text{int}} \\ v_y &= v_G \sin \beta_{\text{int}} \end{aligned} \tag{7}$$

where β_{int} is the sideslip angle calculated by the integration method.

The lateral velocity can be derived by

$$\begin{aligned} \begin{bmatrix} \dot{v}_y(t) \\ \dot{a}_b \end{bmatrix} &= \begin{bmatrix} 0 & -1 \\ 0 & 0 \end{bmatrix} \begin{bmatrix} v_y(t-1) \\ a_b \end{bmatrix} + \begin{bmatrix} 1 \\ 0 \end{bmatrix} (a_y - \omega_z v_x) \\ v_y(t) &= \begin{cases} \begin{bmatrix} 1 & 0 \end{bmatrix} \begin{bmatrix} v_y(t) \\ a_b \end{bmatrix} & \text{if GPS is updated} \\ v_y(t-1) & \text{if GPS is not updated} \end{cases} \end{aligned} \tag{8}$$

where a_b is the measurement bias of the lateral acceleration.

A Kalman filter presented from [31] is applied to integrate the measurements of GPS and IMU, which would reduce the measurement error and avoid the drift of the estimate. The filter is formulated by

$$\begin{aligned} \boldsymbol{L}_{\text{KF}}(k) &= \boldsymbol{P}_{\text{KF}}(k)\boldsymbol{C}^{\text{T}}(\boldsymbol{C}\boldsymbol{P}_{\text{KF}}(k)\boldsymbol{C}^{\text{T}} + \boldsymbol{R}_{\text{KF}})^{-1} \\ \boldsymbol{x}_{\text{KF}}(k) &= \boldsymbol{x}_{\text{KF}}(k) + \boldsymbol{L}_{\text{KF}}(k)(\boldsymbol{y}_{\text{KF}}(k) - \boldsymbol{C}\boldsymbol{x}_{\text{KF}}(k-m)) \\ \boldsymbol{P}_{\text{KF}}(k) &= (\boldsymbol{I} - \boldsymbol{L}_{\text{KF}}(k)\boldsymbol{C}) \end{aligned} \tag{9}$$

where $\boldsymbol{C} = [1, 0]^{\text{T}}$ is the output matrix, $\boldsymbol{x}_{\text{KF}}$ is the state vector, $\boldsymbol{P}_{\text{KF}}$ is the covariance matrix, $\boldsymbol{R}_{\text{KF}}$ is the measurement noise, $\boldsymbol{L}_{\text{KF}}$ is the Kalman gain, $\boldsymbol{y}_{\text{KF}}$ is the output signal which is the lateral velocity and m means the last time step when GPS is updated.

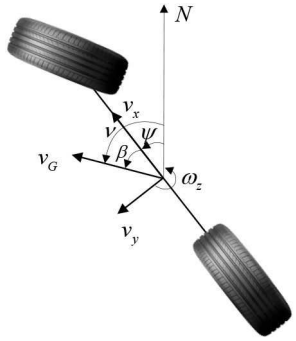

Fig. 1 *Kinematics vehicle model*

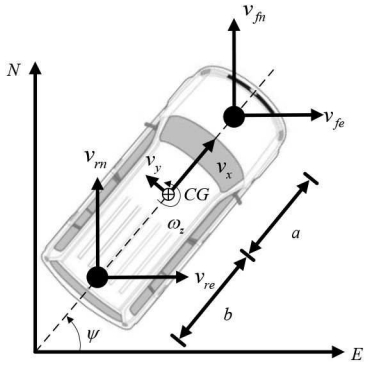

Fig. 2 *DGPS kinematics vehicle model*

The GPS update rate for mass production vehicles is no more than 20 Hz while the control period of a typical vehicle control unit (VCU) is 20 or 10 ms. There is clearly a mismatch here.

3.1.2 DGPS-IMU fusion: Differential global positioning system (DGPS) is a special GPS with two independent antennas, which has a higher update rate. The two independent antennas are installed on the front and rear parts of the vehicle as shown in Fig. 2, where N and E are the North and the East in the earth coordinate [41, 100].

Based on [41, 100], the DGPS-IMU fusion method is established. Using the signals from the two antennas, the relationship between the velocity and yaw rate at CG and the installation positions can be given by

$$\begin{cases} v_{fe} = v_x \cos\psi - (v_y + a\omega_z)\sin\psi \\ v_{fn} = v_x \sin\psi + (v_y + a\omega_z)\cos\psi \\ v_{re} = v_x \cos\psi - (v_y - b\omega_z)\sin\psi \\ v_{rn} = v_x \sin\psi + (v_y - b\omega_z)\cos\psi \end{cases} \tag{10}$$

where v_{fe} is the eastbound velocity measured by the front receiver, v_{fn} is the northbound velocity measured by the front receiver, v_{re} is the eastbound velocity measured by the rear receiver and v_{rn} is the northbound velocity measured by the rear receiver.

The sideslip angle can be further derived by

$$\begin{cases} v_x = v_{fe}\cos\psi + v_{fn}\sin\psi \\ v_y = v_{re}\sin\psi + v_{rn}\cos\psi \end{cases} \tag{11}$$

$$\psi = \arctan\left(\frac{v_{fe} - v_{re}}{v_{rn} - v_{fn}}\right) \tag{12}$$

With the two independent GPS antennas, the yaw angle can be directly calculated. The yaw angle is directly derived instead of finding the singular points of (10), which is more computationally efficient.

The eastbound and northbound velocities v_e and v_n can be derived by

$$\begin{cases} v_e = \dfrac{b}{a+b}v_{fe} + \dfrac{a}{a+b}v_{re} \\ v_n = \dfrac{b}{a+b}v_{fn} + \dfrac{a}{a+b}v_{rn} \end{cases} \tag{13}$$

The heading angle of the vehicle can be calculated based on the eastbound and northbound velocities by

$$\nu = \arctan\left(\frac{v_n}{v_e}\right) \tag{14}$$

Then, the sideslip angle can be derived based on (2).

The first two equations in (10) are used when the front GPS receiver has measurement updates, and the latter two equations are used when the rear GPS receiver has measurement updates. As the two GPS receivers update themselves independently, an asynchronisation problem exists. Thus, it is necessary to update the output signal when either receiver has refreshed. In this way, the DGPS update rate may become twice of the update rate of the conventional GPS.

3.2 Dynamics-based methods

EKF- and UKF-based observers combined with optimised tire models are introduced here for vehicle sideslip angle estimation as the representatives of the dynamics-based method. It is worth mentioning that the dynamics-based methods presented in this study are selected from [74, 82, 100].

The observers are established based on a five degrees of freedom (5-DOF) vehicle model as illustrated in Fig. 3, which includes the longitudinal, lateral and yaw motions of the vehicle and the rotations of the front and rear wheels, where F_{fx} and F_{rx} are the longitudinal forces of the front and rear wheels.

Based on the D'Alembert principle, the equations of motion are given as

$$ma_y = 2F_{fy}\cos\delta + 2F_{ry} \tag{15}$$

$$I_z\dot{\omega}_z = 2aF_{fy}\cos\delta - 2bF_{ry} \tag{16}$$

$$a_y = \dot{v}_y + \omega_z v_x \tag{17}$$

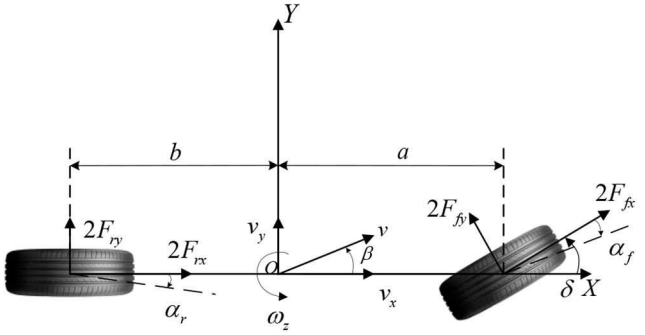

Fig. 3 *5-DOF dynamic vehicle model*

$$a_x = \dot{v}_x - \omega_z v_y \tag{18}$$

where I_z is the rotational inertia of the vehicle, and a_x and a_y are the longitudinal and lateral accelerations at CG.

The sideslip angles of the front and rear tires can be derived by

$$\alpha_f = \beta + \frac{a\omega_z}{v_x} - \delta \tag{19}$$

$$\alpha_r = \beta - \frac{b\omega_z}{v_x} \tag{20}$$

Based on (1) and (15)–(20), the equations of motion of the vehicle can be derived as [82]

$$\dot{v}_y = \frac{\beta_1}{v_x} v_y + \left(\frac{\beta_2}{v_x} - v_x\right)\omega_z + \beta_3 \delta \tag{21}$$

$$\dot{\omega}_z = \frac{\beta_4}{v_x} v_y + \frac{\beta_5}{v_x}\omega_z + \beta_6 \delta \tag{22}$$

$$\dot{v}_x = a_x + \omega_z v_y \tag{23}$$

where $\beta_1 = -2(C_f\cos\delta + C_r)/m$, $\beta_2 = 2(-C_f a\cos\delta + C_r b)/m$, $\beta_3 = 2C_f\cos\delta/m$, $\beta_4 = 2(C_f a\cos\delta + C_r b)/I_z$, $\beta_5 = -2(C_f a^2\cos\delta + C_r b^2)/I_z$, $\beta_6 = 2C_f a\cos\delta/I_z$.

Tire model selection has significant impact on overall accuracy of the vehicle model. To promote the accuracy, an adaptive method for tire cornering stiffness identification is introduced as

$$\begin{aligned} mba_y + I_z\dot{\omega}_z = {} & m(a+b)a_y\frac{C_f}{C_f + C_r} \\ & +2(a+b)\left[\delta - \frac{(a+b)\omega_z}{v_x}\right]\frac{C_f C_r}{C_f + C_r} \end{aligned} \tag{24}$$

The cornering stiffness of the rear tires is proportional to that of the front tires, which is given by

$$C_r = k_c C_f \tag{25}$$

where k_c is the proportion factor.

The RLS is employed to calculate the cornering stiffness, which is given by

$$\boldsymbol{\theta}(k) = \hat{C}_f(k) \tag{26}$$

$$\boldsymbol{\varphi}^{\mathrm{T}}(k) = 2\frac{k_C(a+b)}{1+k_C}\left[\delta(k) - \frac{(a+b)\omega_z(k)}{v_x(k)}\right] \tag{27}$$

$$\boldsymbol{y}_{\mathrm{RLS}}(k) = ma_y(k)\frac{k_C b - a}{1+k_C} + I_z\dot{\omega}_z(k) \tag{28}$$

where $\boldsymbol{\theta}(k)$ is the variable to be observed, $\boldsymbol{\varphi}^{\mathrm{T}}(k)$ is the recursive factor, $\boldsymbol{y}_{\mathrm{RLS}}(k)$ is the output vector and $\dot{\omega}_z$ is the yaw acceleration, which can be measured by IMU.

The iteration process is as follows:

$$\boldsymbol{K}_{\mathrm{RLS}}(k) = \frac{\boldsymbol{P}_{\mathrm{RLS}}(k-1)\boldsymbol{\varphi}(k)}{\lambda_f \boldsymbol{I} + \boldsymbol{\varphi}^{\mathrm{T}}(k)\boldsymbol{P}_{\mathrm{RLS}}(k-1)\boldsymbol{\varphi}(k)} \tag{29}$$

$$\boldsymbol{P}_{\mathrm{RLS}}(k) = \frac{1}{\lambda_f}(\boldsymbol{I} - \boldsymbol{K}_{\mathrm{RLS}}(k)\boldsymbol{\varphi}^{\mathrm{T}}(k))\boldsymbol{P}_{\mathrm{RLS}}(k-1) \tag{30}$$

$$\boldsymbol{\theta}(k) = \boldsymbol{\theta}(k-1) + \boldsymbol{K}_{\mathrm{RLS}}(k)(\boldsymbol{y}_{\mathrm{RLS}}(k) - \boldsymbol{\varphi}^{\mathrm{T}}(k)\boldsymbol{\theta}(k-1)) \tag{31}$$

where $\boldsymbol{K}_{\mathrm{RLS}}$ is the Kalman gain, $\boldsymbol{P}_{\mathrm{RLS}}$ is the covariance matrix, $\boldsymbol{I}$ is the unit matrix, and λ_f is the forgetting factor.

Based on the adaptive cornering stiffness factor, β_i ($i = 1, 2, 3, 4, 5, 6$) become time-varying parameters.

Then, the state and observe equations of the sideslip angle observer can be derived as

$$\boldsymbol{x}_k = f(\boldsymbol{x}_{k-1}, \boldsymbol{u}_{k-1}) + \boldsymbol{w}_{k-1} \tag{32}$$

$$\boldsymbol{z}_k = h(\boldsymbol{x}_k) + \boldsymbol{v}_k \tag{33}$$

where f is a non-linear state equation based on (21)–(23), h is the observation equation, $\boldsymbol{x}_k = [v_y(k), \omega_z(k), v_x(k)]^{\mathrm{T}}$ is the state vector, $\boldsymbol{z}_k = [\hat{\omega}_z(k), \hat{v}_x(k)]^{\mathrm{T}}$ is the observation vector, $\boldsymbol{u}_k = [\delta(k), a_x(k), a_y(k)]^{\mathrm{T}}$ is the input vector, $\boldsymbol{w}_k$ is the process noise with the covariance of $\boldsymbol{Q}_k$ and $\boldsymbol{v}_k$ is the measurement noise with the covariance of $\boldsymbol{R}_k$.

Due to the existence of sensor noises, an EKF filter is used to improve the stability of the observer.

The equations of state update are given by

$$\hat{\boldsymbol{x}}_{k|k-1} = f(\boldsymbol{x}_{k-1}, \boldsymbol{u}_{k-1}) + \boldsymbol{w}_{k-1} \tag{34}$$

$$\boldsymbol{P}_{k|k-1} = \boldsymbol{F}_{k|k-1}\boldsymbol{P}_{k|k-1}\boldsymbol{P}^{\mathrm{T}}_{k|k-1} + \boldsymbol{Q}_{k-1} \tag{35}$$

where $\boldsymbol{F}_{k|k-1}$ is the Jacobian matrix of the state equation with respect to state $\boldsymbol{x}_{k|k-1}$, and $\boldsymbol{P}$ is the covariance matrix.

The equations of measurement update are given by

$$\boldsymbol{K}_k = \boldsymbol{P}_{k|k-1}\boldsymbol{H}_k^{\mathrm{T}}(\boldsymbol{H}_k\boldsymbol{P}_{k|k-1}\boldsymbol{H}_k^{\mathrm{T}} + \boldsymbol{R}_k)^{-1} \tag{36}$$

$$\hat{\boldsymbol{x}}_k = \hat{\boldsymbol{x}}_{k|k-1} + \boldsymbol{K}_k(\boldsymbol{y}_k - \boldsymbol{z}_{k|k-1}) \tag{37}$$

$$\boldsymbol{P}_k = (\boldsymbol{I} - \boldsymbol{K}_k\boldsymbol{H}_k)\boldsymbol{P}_{k|k-1} \tag{38}$$

where $\boldsymbol{H}_k$ is the Jacobian matrix of the observation equation with respect to state $\boldsymbol{x}_{k-1}$, $\boldsymbol{K}_k$ is the Kalman gain, $\boldsymbol{y}_k = [\omega_z(k), v_x(k)]^{\mathrm{T}}$ is the measurement in which the yaw rate is measured by IMU and the longitudinal velocity by the wheel speed sensor.

Table 1 Training manoeuvre

steering angle	90° 0.25 Hz sinusoidal input
speed	20–130 km/h
friction coefficient	0.4, 0.7, 1.0

Table 2 First row of covariance matrix

Covariance	Sideslip angle
sideslip angle	1
longitudinal velocity	**$-3.080*10^{-4}$**
left front wheel speed	−0.0040
left rear wheel speed	−0.0111
right front wheel speed	0.0042
right rear wheel speed	0.0115
longitudinal acceleration	−0.0070
lateral acceleration	−0.5241
yaw rate	−0.2320
roll rate	−0.0565
steering angle	−0.2001

The UKF is also widely employed for sideslip angle estimation. In the UKF, the probability density distribution of the non-linear function and the posterior probability density of the state are approximated by a series of samples, which maintains high-order terms. The sigma points are generated by

$$\boldsymbol{\chi}_{k-1|k-1}=\begin{cases}\bar{\boldsymbol{x}}^i_{k-1|k-1}, & i=0\\ \bar{\boldsymbol{x}}^i_{k-1|k-1}+\sqrt{(n+\lambda)\bar{\boldsymbol{P}}^i_{k-1|k-1}}, & i=1,\ldots,n\\ \bar{\boldsymbol{x}}^i_{k-1|k-1}-\sqrt{(n+\lambda)\bar{\boldsymbol{P}}^i_{k-1|k-1}}, & i=n+1,\ldots,2n\end{cases} \quad (39)$$

The states are predicted by

$$\boldsymbol{\chi}^i_{k|k-1}=f_i(\boldsymbol{\chi}_{k-1|k-1},\boldsymbol{u}_{k-1}) \quad (40)$$

$$\hat{\boldsymbol{x}}^i_{k|k-1}=\sum_{i=0}^{2n}W_i^m\boldsymbol{\chi}^i_{k|k-1} \quad (41)$$

$$\boldsymbol{\gamma}^i_{k|k-1}=h_i(\boldsymbol{\chi}^i_{k|k-1}) \quad (42)$$

$$\hat{\boldsymbol{y}}^i_{k|k-1}=\sum_{i=0}^{2n}W_i^m\boldsymbol{\gamma}^i_{k|k-1} \quad (43)$$

The covariance is updated by

$$\hat{\boldsymbol{P}}^i_{k|k-1}=\sum_{i=0}^{2n}W_i^c(\boldsymbol{\chi}^i_{k|k-1}-\hat{\boldsymbol{x}}_{k|k-1})(\boldsymbol{\chi}^i_{k|k-1}-\hat{\boldsymbol{x}}_{k|k-1})^{\mathrm{T}}+\boldsymbol{Q}_k \quad (44)$$

The measurement update is given by

$$\boldsymbol{P}_{z,k}=\sum_{i=0}^{2n}W_i^c(\boldsymbol{\gamma}^i_{k|k-1}-\hat{\boldsymbol{z}}^i_{k|k-1})(\boldsymbol{\gamma}^i_{k|k-1}-\hat{\boldsymbol{z}}^i_{k|k-1})^{\mathrm{T}}+\boldsymbol{R}_k \quad (45)$$

$$\boldsymbol{P}_{xz,k}=\sum_{i=0}^{2n}W_i^c(\boldsymbol{\chi}^i_{k|k-1}-\hat{\boldsymbol{x}}^i_{k|k-1})(\boldsymbol{\gamma}^i_{k|k-1}-\hat{\boldsymbol{z}}^i_{k|k-1})^{\mathrm{T}} \quad (46)$$

$$\boldsymbol{K}_k=\boldsymbol{P}_{xz,k}\boldsymbol{P}^{-1}_{z,k} \quad (47)$$

$$\hat{\boldsymbol{x}}_k=\hat{\boldsymbol{x}}_{k|k-1}+\boldsymbol{K}_k(\boldsymbol{y}_k-\hat{\boldsymbol{y}}_{k|k-1}) \quad (48)$$

where $\boldsymbol{\chi}_{k-1|k-1}$ and $\boldsymbol{\gamma}_{k|k-1}$ are the sigma points constructed from the unscented transformation, and W_i^m and W_i^c are the weights, which are given by

$$\begin{cases}W_0^m=\dfrac{\kappa}{\kappa+n}\\ W_0^c=\dfrac{\kappa}{\kappa+n}+(1-\alpha_w^2+\beta_w)\\ W_i^m=W_i^c=\dfrac{\kappa}{2(\kappa+n)}, \quad i=1,\ldots,2n\end{cases} \quad (49)$$

where $\kappa=\alpha_w^2(n+\lambda)-n$, α_w, λ and β_w are the factors that influence the performance of the UKF.

3.3 NN-based method

The NN-based method is based on our previous publication [101]. The relationship between sideslip angle and other vehicle parameters is difficult to be fully and accurately represented. The longitudinal vehicle velocity can be acquired via the accurate knowledge of rotational speed and effective radius of wheels. The longitudinal velocity, longitudinal acceleration, lateral acceleration, roll rate and yaw rate of the vehicle, the steering angle of the front wheels and the rotational speeds of wheels may have influence on vehicle sideslip angle. Among these motion states, the wheel speeds can be obtained from the wheel speed sensors, the longitudinal speed can be obtained from the VCU based on the wheel speeds, the longitudinal acceleration, lateral acceleration, yaw rate and roll rate of the vehicle can be measured by IMU and the steering angle can be measured by the steering angle encoder.

The CarSim software is used to acquire the raw data to train the NN. As shown in Table 1, extreme manoeuvres are executed in order to obtain sufficient data for model training under critical conditions [102].

Various sensor signals that are implicitly correlated with vehicle sideslip angle are available from CarSim. In order to reduce the number of model input features and improve computational efficiency, a selection of signals with high correlation is necessary. The PCA method is used to verify whether the parameters have high relevance with sideslip angle [95]. In this work, since the PCA is not suitable for online estimation in the VCU, the covariance matrix is used to analyse the correlation between different parameters and vehicle sideslip angle, in which high eigenvalue indicates high correlation and vice versa.

Table 2 shows that the first row of the covariance matrix between the selected input features and the outputs. It is obvious that the eigenvalue of the longitudinal velocity is obviously smaller than the others, so the longitudinal velocity is removed from the input features.

A non-linear autoregressive exogenous NN (NARX-NN) is proposed for vehicle sideslip angle estimation, and its structure is illustrated in Fig. 4. The vehicle sideslip angle indicates the lateral stability state of the vehicle, which can be influenced by the inputs

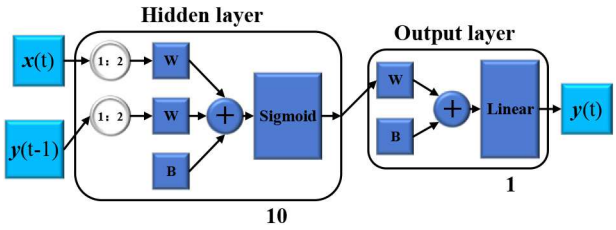

Fig. 4 *Structure of NARX NN*

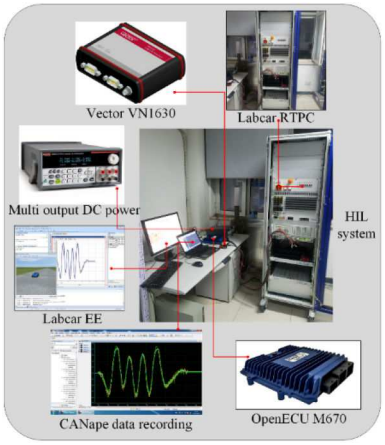

Fig. 5 *HIL test system for vehicle sideslip angle estimation evaluation*

at several previous time steps. Therefore, a time delay module is also included.

Then, the NARX-NN can be described as a function of the estimated sideslip angle with respect to other input features by

$$\begin{aligned}\hat{\beta}(k) = f_{\text{NARX}}(&\omega_{fr}(k), \omega_{rr}(k), \omega_{fl}(k), \omega_{fl}(k),\\ &a_x(k), a_y(k), \omega_z(k), \omega_x(k), \delta(k), \ldots\\ &\omega_{fr}(k-n_d), \omega_{rr}(k-n_d), \omega_{fl}(k-n_d), \omega_{fl}(k-n_d),\\ &a_x(k-n_d), a_y(k-n_d), \omega_z(k-n_d), \omega_x(k-n_d), \delta(k-n_d))\end{aligned} \tag{50}$$

where $\omega_{i,j}$ are the rotational wheel speeds with $i = f, r$ and $j = l, r$, ω_x is the roll rate and n_d represents the number of delayed time steps. A larger n_d can contribute to better robustness, but the instantaneity may be compromised if it is too large.

4 Comparison studies

To compare the performance of the above-mentioned sideslip angle estimators, a HIL system is set up as shown in Fig. 5. The CarSim software is utilised to simulate vehicle response with high fidelity. The ETAS Labcar is employed as a real-time PC in which the established vehicle models are run. A rapid prototyping controller PI OpenECU M670 is used as the VCU, in which the estimators are implemented. The vector VN1630 is used for data logging.

Five commonly used estimators are systematically examined and compared. They are the GPS-IMU, DGPS-IMU, EKF-, UKF- and NN-based estimators, among which the GPS-IMU and DGPS-IMU represent the kinematics-based methods and the EKF- and UKF-based estimators exemplify the dynamics-based approaches. Four typical manoeuvres including the double lane change (DLC), Slalom, Fishhook and roundabout network are used to comprehensively represent the driving situations under which sideslip angle estimators are necessarily executed. The selected manoeuvres can cover typical driving conditions in which the ACSs could be triggered once the sideslip angle is well estimated. Various road adhesion coefficients ranging from 0.4 to 0.9 are used in the simulation to examine the performance of each estimator under snow-covered, wet and dry road conditions. The vehicle velocities range from 30 to 130 km/h and are set constant throughout each test process. Combined with different vehicle velocities and road adhesion coefficients, the test scenarios are sufficient under each driving manoeuvre. In addition, it is worth mentioning that the road slope is set zero and the road surface is set to be asphalt.

The root-mean-square error (RMS) is employed to delineate the estimation accuracy, which is given by

$$\text{RMS}_j = \sqrt{\frac{\sum_{i=1}^{N_c}(\beta_{\text{real},i} - \beta_{j,i})^2}{N_c}} \tag{51}$$

where N_c is the sampled points, β_{real} is the real sideslip angle and β_j is the estimated sideslip angle with $j = 1, 2, ..., 5$.

To further evaluate the estimation performance, the mean absolute error (MAE) is also employed, which is given by

$$\text{MAE}_j = \sum_{i=1}^{N_c}\left|\frac{\beta_{\text{real},i} - \beta_{j,i}}{\beta_{\text{real},i}}\right|\frac{1}{N_c} \tag{52}$$

The simulation results are illustrated in figures in order to intuitively illustrate the comparison results. The quantitative results are given in Table 3.

The performance of each estimator is quantitatively compared regarding accuracy, robustness and generalisation capability with the detailed results depicted in Table 4. The generalisation capability refers to the applicability of an estimator when used for other vehicle models and/or under different test conditions. The accuracy is evaluated by the MAE under all test manoeuvres, and the robustness is assessed by the variance of the MAE, which is given by

$$D(\beta) = \frac{\sum(\beta - \bar{\beta})}{N_m} \tag{53}$$

where N_m is the number of test manoeuvres and $\bar{\beta}$ is the mean value of the estimated sideslip angle.

4.1 Double lane change manoeuvre

A DLC maneuverer is constructed according to the Standard ISO 3888-1 as shown in Fig. 6. A set of vehicle velocities ranging from 30 to 90 km/h and two road friction coefficients are used to evaluate the estimation performance of each estimator.

Table 3 MAE of each estimator under different manoeuvres

Velocity, km/h	GPS/IMU	DGPS/IMU	EKF	UKF	NN
DLC $\mu = 0.8$					
30	0.049321	0.042416	0.03418	0.019618	0.002113
40	0.054098	0.379924	0.058228	0.037732	0.00406
50	0.072036	0.320413	0.124998	0.111195	0.009414
60	0.139108	0.516144	0.560052	0.529595	0.031091
70	0.064926	0.493098	0.360492	0.354245	0.022603
80	0.03039	0.17454	0.214679	0.215412	0.015415
90	0.018509	0.054894	0.1339	0.137134	0.013145
100	0.017174	0.047932	0.173957	0.171724	0.01647
110	0.013952	0.036077	0.213866	0.207099	0.017347
120	0.011309	0.039288	0.218193	0.205826	0.017817
130	0.009234	0.056576	0.200477	0.19815	0.018419
DLC $\mu = 0.4$					
30	0.049434	0.042601	0.03315	0.01858	0.002118
40	0.055223	0.377564	0.068979	0.047462	0.004143
50	0.080687	0.354872	0.141243	0.130651	0.010541
60	0.181556	1.530162	0.646778	0.616943	0.040555
70	0.274547	3.177536	1.813273	1.762195	0.095825
80	0.069847	0.499086	0.640781	0.631784	0.035643
90	0.03435	0.08255	0.410646	0.408886	0.024908
100	0.020232	0.045072	0.284928	0.291391	0.019581
110	0.013477	0.032494	0.208336	0.206422	0.016786
120	0.010156	0.029087	0.165358	0.164405	0.016069
130	0.008394	0.026981	0.141057	0.126367	0.017127
slalom $\mu = 0.8$					
30	0.041371	0.078264	0.03936	0.032639	0.00193
40	0.051545	0.085238	0.099328	0.097499	0.003515
50	0.098761	0.116205	0.560216	0.603349	0.010245
60	0.081991	0.091533	1.10461	1.091249	0.014279
70	0.036959	0.047446	1.098476	0.966862	0.010359
80	0.023481	0.037748	0.892711	0.706615	0.009676
90	0.016909	0.036532	0.767371	0.766771	0.009408
100	0.013412	0.032832	0.412708	0.3866	0.009329
110	0.011462	0.031286	0.383302	0.173209	0.009494
120	0.010287	0.029643	0.358744	0.351531	0.009853
130	0.009449	0.028441	0.339238	0.125981	0.010415
slalom $\mu = 0.4$					
30	0.040952	0.080293	0.045223	0.036528	0.001918
40	0.044801	0.08007	0.107913	0.073515	0.003114
50	0.063518	0.084623	0.208011	0.201381	0.006557
60	0.163779	0.164713	1.019424	0.884979	0.023939
70	0.042387	0.061588	0.354966	0.325933	0.008608
80	0.023595	0.066823	0.254087	0.223668	0.006773
90	0.01815	0.059842	0.245216	0.211265	0.007111
100	0.01535	0.055851	0.242591	0.220523	0.007824
110	0.013448	0.060041	0.236715	0.194368	0.008616
120	0.012311	0.05617	0.23381	0.194344	0.009653
130	0.01145	0.053568	0.22865	0.228285	0.010925
fishhook $\mu = 0.7$					
30	0.023982	0.055685	0.073404	0.05383	0.007956
40	0.062771	0.09176	2.556534	2.411454	0.025931
fishhook $\mu = 0.9$					
30	0.023442	0.054654	0.065543	0.046463	0.008264
40	0.061823	0.067794	0.144647	0.118781	0.00764
roundabout network $\mu = 0.6$					
40	0.046894	0.035911	0.042204	0.04464	0.002716
50	0.182895	0.053224	0.216158	0.195106	0.00578
roundabout network $\mu = 0.9$					
40	0.046913	0.035955	0.106318	0.070566	0.00512
50	0.182895	0.053224	0.221151	0.168461	0.009505

Table 4 Quantitative evaluations of the estimators

Estimators	Accuracy	Robustness	Generalisation
GPS-IMU	0.000358	0.000358	high
DGPS-IMU	0.029240	0.029240	high
EKF -based	0.045002	0.045002	high
UKF-based	0.040688	0.040688	high
NN-based	0.000014	0.000014	low

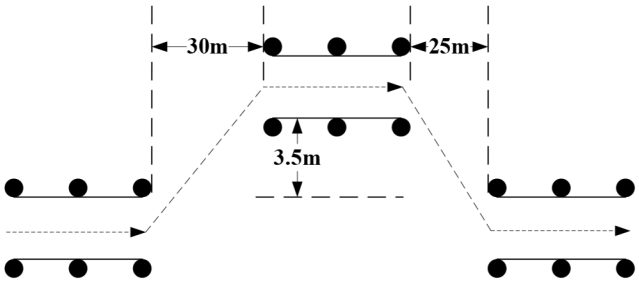

Fig. 6 *DLC manoeuvre*

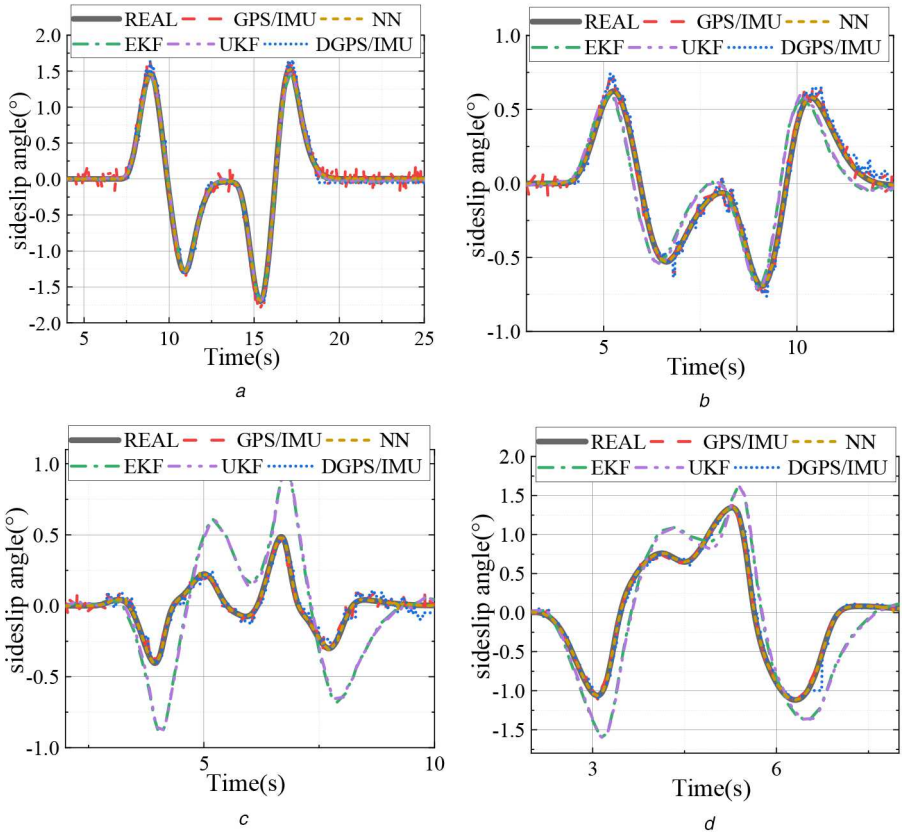

Fig. 7 *Estimation results under the double lance change manoeuvre with the road friction coefficient of 0.8 at* ***(a)*** 30 km/h, ***(b)*** 50 km/h, ***(c)*** 70 km/h, ***(d)*** 90 km/h

The estimation results under the high-adhesion road condition and different vehicle velocities are shown in Fig. 7. It can be seen that the vehicle velocity has significant impact on the performance of all estimators. All the estimators can yield satisfying results at the low velocity of 30 km/h as the MSE of each estimator is well below 5%, which is superior than the estimation results reported in [31, 57]. More detailed results can be found in the Table 3. At the velocity of 30 km/h, the tires still work in the linear region and the dynamics model is accurate. That can explain why the dynamics-based estimators are of high accuracy. For the kinematics-based methods, the estimation accuracy is also within an acceptable range despite low SNR may to a limited extent curtail the performance. The dynamics-based estimators exhibit an obvious estimation lag when the velocity reaches 50 km/h. At the velocity of 70 km/h, the dynamics-based estimators completely fail while the kinematics-based estimators still have high estimation accuracy and the measurement noise has diminishing influence with the increasing vehicle velocity. In particular, the DGPS-IMU method outperforms the GPS-IMU method due to its higher update frequency. The NN-based estimator yields the best estimation performance at all velocities.

In order to further evaluate the estimation performance under the low road adhesion conditions, the DLC maneuverer is also performed with the road friction coefficient of 0.4 at the velocities of 70 and 90 km/h. The results are shown in Fig. 8. It can be seen that the dynamics-based estimators cannot achieve effective estimation at both velocities while the kinematics- and NN-based estimators stage good estimation performance.

The RMSs of the presented estimators during the DLC manoeuvre at different vehicle velocities and road adhesion

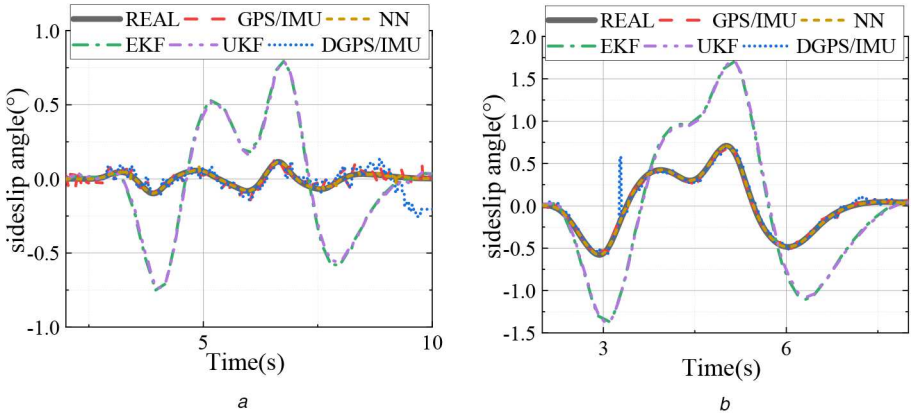

Fig. 8 *Estimation results under the double lance change manoeuvre with the road friction coefficient of 0.4 at* ***(a)*** 70 km/h, ***(b)*** 90 km/h

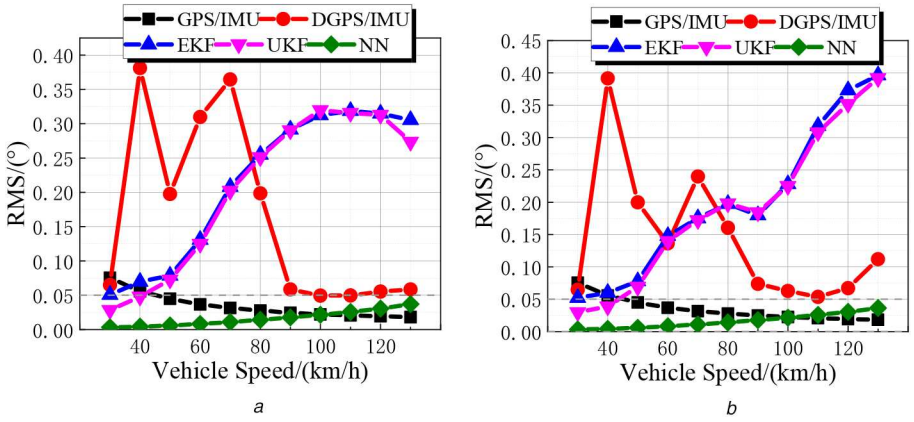

Fig. 9 *Estimation RMSs during the DLC manoeuvre under the road friction coefficient of* ***(a)*** $\mu = 0.4$, ***(b)*** $\mu = 0.8$

conditions are depicted in Fig. 9. It can be seen that the EKF- and UKF-based estimators are effective only when the vehicle velocity is well below 50 km/h, and the UKF has higher accuracy than the EKF. The main reason lies in that the tire enters into the non-linear region as the vehicle velocity surpasses 50 km/h during the cornering. As well, the dynamics-based estimators are highly dependent on the accuracy of the employed tire model. In contrast, the NN-based estimator has the best estimation performance under all the selected velocities, but its estimation error tends to increase with the incrementing vehicle velocity. Besides, both the GPS-IMU and DGPS-IMU can realise sideslip angle estimation under different velocities while the estimation accuracy of the GPS-IMU exhibits a continuous improvement along with the increasing vehicle velocity. This can be ascribed to the enlarged SNR of GPS signal.

4.2 Slalom manoeuvre

The slalom manoeuvre serves to assess the performance of the estimators under continuous cornering situations. A sinusoidal excitation with an amplitude of 90° and a frequency of 0.25 Hz are imposed on the steering wheel. Again, the vehicle velocities are set from 30 to 90 km/h, and the road friction coefficients of 0.4 and 0.8 are utilised.

The estimation results under the high road adhesion condition are shown in Fig. 10. It can be seen that their estimation performance is similar to that under the double lance change manoeuvre. The dynamics-based estimators only avail at the velocity of 30 km/h, while the kinematics- and NN-based are valid under all the selected velocities.

Under the low road adhesion condition, the kinematics- and NN-based estimators perform well in parallel with that under the high road adhesion condition. The dynamics-based estimators excel under the low road adhesion condition in comparison with that under the high road adhesion condition. The non-linear characteristics of tires become more profound with the increasing lateral tire force. Under low road adhesion conditions, the maximum lateral tire force is smaller than that under high road adhesion conditions. Thus, the tire can exhibit more non-linear characteristics under high road adhesion conditions than that under low road adhesion conditions. This may account for the performance gap illustrated by Figs. 10 and 11.

The RMSs during the Slalom manoeuvre under different vehicle velocities and road adhesion conditions are illustrated in Fig. 12. It can be seen that all the estimators exhibit similar performance with that under the DLC manoeuvre. However, the DGP-IMU estimator performs much better in the Slalom manoeuvre than in the DLC manoeuvre. This may result from a smaller proportion of the straight driving.

4.3 Fishhook manoeuvre

A fishhook manoeuvre is constructed as shown in Fig. 13. The employment of the fishhook manoeuvre is to assess the performance of the estimators in sharp steering situations. The vehicle velocities are set 40 and 50 km/h, and the road friction coefficients of 0.7 and 0.9 are utilised.

The estimation results are shown in Fig. 14. It can be seen that the NN-based estimator yields the best accuracy. Both the kinematics- and dynamics-based estimators can overall realise sideslip angle estimation; but there are obvious deviations on the straight driving parts. Upon a close observation, the GPS-IMU estimator outperforms the DGPS-IMU estimator on the straight driving parts while vice versa on the cornering parts. The dynamics-based estimators are only effective at the vehicle velocity of 30 km/h, and the UKF has higher accuracy than the EKF. When the velocity is above 40 km/h, both dynamics-based estimators fail to converge.

The RMSs during the Fishhook manoeuvre under different vehicle velocities and road adhesion conditions are illustrated in

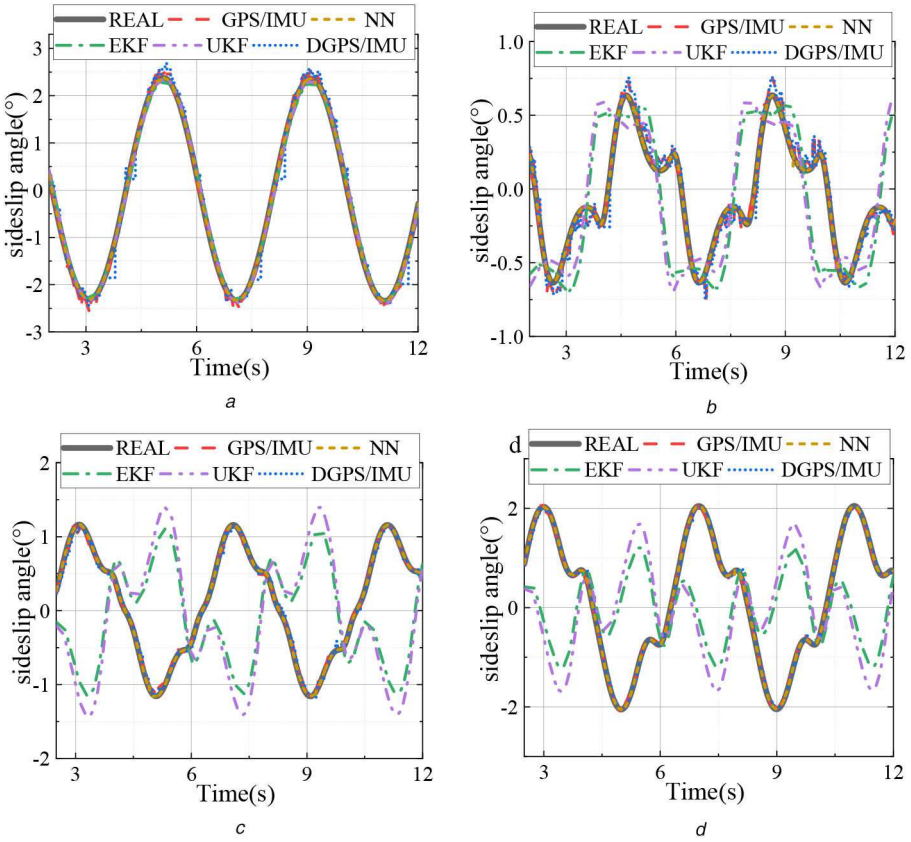

Fig. 10 *Estimation results under the Slalom manoeuvre with the road friction coefficient of 0.8 at*
(a) 30 km/h, ***(b)*** 50 km/h, ***(c)*** 70 km/h, ***(d)*** 90 km/h

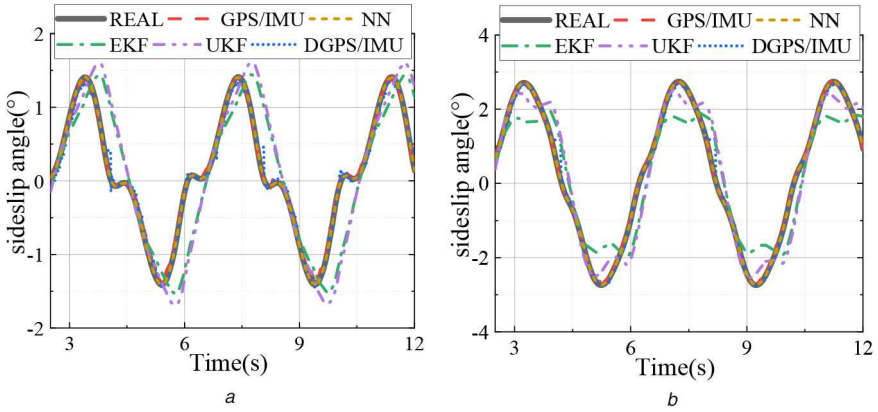

Fig. 11 *Estimation results under the Slalom manoeuvre with the road friction coefficient of 0.4 at*
(a) 70 km/h, ***(b)*** 90 km/h

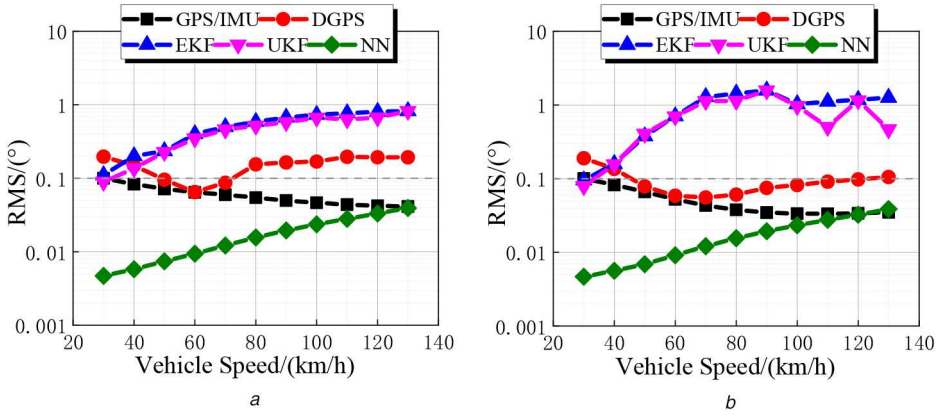

Fig. 12 *Estimation RMSs during the Slalom manoeuvre under the road friction coefficient of*
(a) $\mu = 0.4$, ***(b)*** $\mu = 0.8$

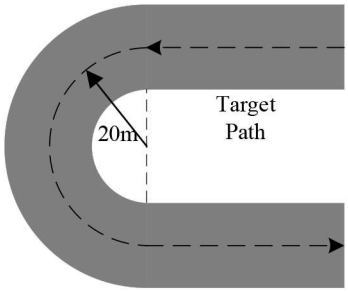

Fig. 13 *Fishhook manoeuvre*

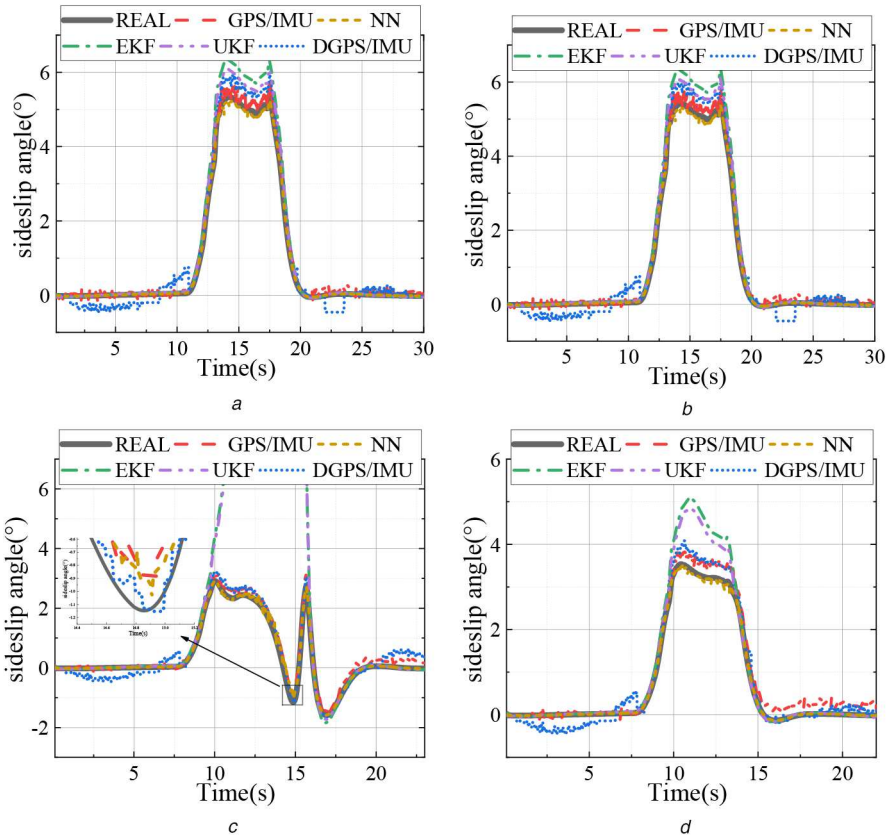

Fig. 14 *Estimation results under the Fishhook manoeuvre with*
(a) 30 km/h, $\mu = 0.7$, ***(b)*** 30 km/h, $\mu = 0.9$, ***(c)*** 40 km/h, $\mu = 0.7$, ***(d)*** 40 km/h, $\mu = 0.9$

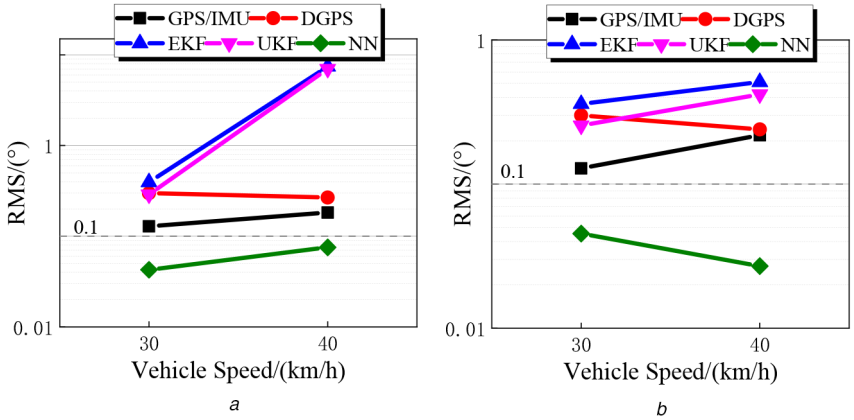

Fig. 15 *Estimation RMSs during the Fishhook manoeuvre under the road friction coefficient of*
(a) $\mu = 0.7$, ***(b)*** $\mu = 0.9$

Fig. 15. When the vehicle velocity is at 30 km/h, each method has acceptable estimation performance. However, when the velocity is well above 40 km/h, the dynamics-based estimators fail especially when the drifting appears on low adhesion roads. The NN-based estimator has better estimation accuracy than the other estimators.

4.4 Roundabout network manoeuvre

A roundabout network is constructed as shown in Fig. 16. It is to simulate the continuous and large cornering radius scenarios. The velocities are set 40 and 50 km/h, and the friction coefficients of 0.6 and 0.9 are utilised.

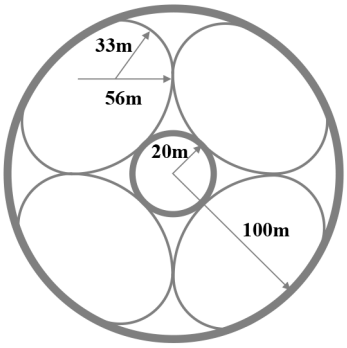

Fig. 16 *Roundabout network manoeuvre*

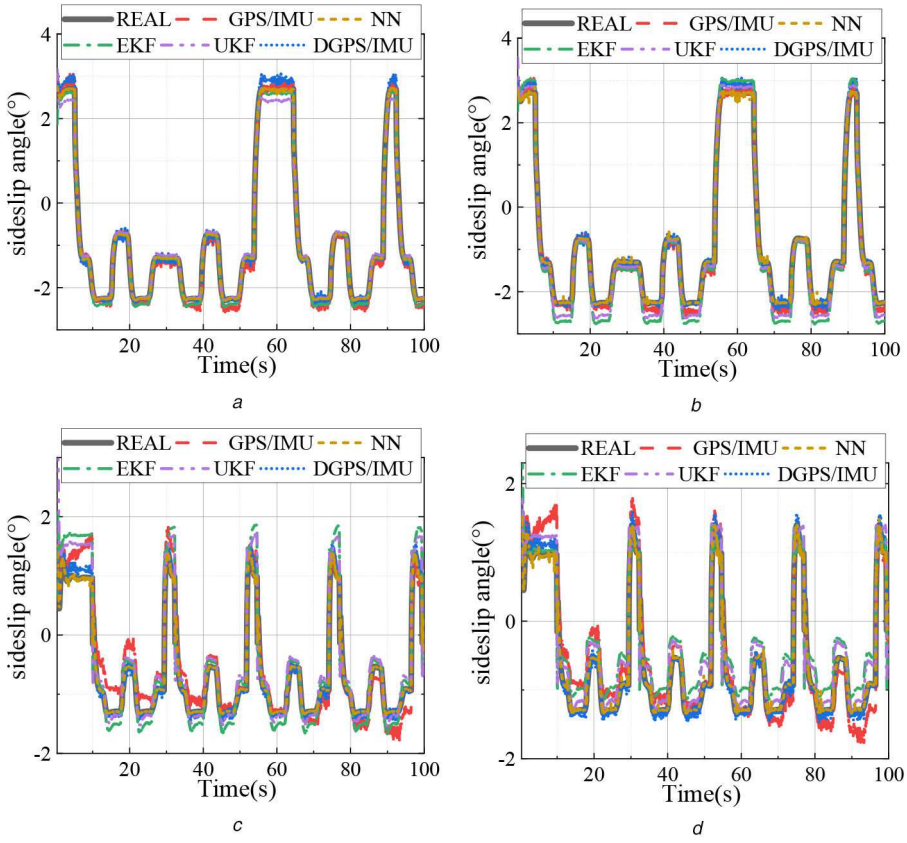

Fig. 17 *Estimation results under the Roundabout network manoeuvre with* ***(a)*** 40 km/h, $\mu = 0.6$, ***(b)*** 40 km/h, $\mu = 0.9$, ***(c)*** 50 km/h, $\mu = 0.6$, ***(d)*** 50 km/h, $\mu = 0.9$

The results during the roundabout network manoeuvre are shown in Fig. 17. It can be seen that the EKF, UKF and GPS-IMU estimators are sensitive to the increasing vehicle velocity. At the velocity of 40 km/h, all the estimators can yield satisfying estimation results as the RMS error of each estimator is under 0.132. However, the dynamics-based estimators at the velocity of 50 km/h have larger biases than that at the velocity of 40 km/h. The DGPS-IMU estimator shows good robustness to the variations of velocity and road adhesion. Still, the NN-based estimator yields the best estimation performance.

The RMSs during the Roundabout network manoeuvre under different vehicle velocities and road adhesion conditions are illustrated in Fig. 18. Also, the NN-based estimator exhibits the best performance under all the selected velocities and road adhesion coefficients. The dynamics-based estimators have similar performance with that under the Fishhook manoeuvre. The DGPS-IMU estimator illustrates robust results with varied velocities. In contrast, the GPS-IMU estimator has a continuous performance degradation along with the increasing vehicle velocity.

A further quantitative evaluation is given in Table 4. The accuracy is evaluated by the MAE and the robustness is assessed by the variance of the MAE under each manoeuvre. In general, the accuracy and robustness of each estimator exhibit a similar pattern. That is, the NN estimator stages the best performance regarding accuracy and robustness relative to the other estimators while the GPS-IMU estimator comes secondary. The DGPS-IMU and dynamics-based estimators perform at the same level. The straight-line driving part notably compromises the overall accuracy of the DGPS-IMU estimator due to small yaw rate as explained in Section 3.1.2. The poor performance of the dynamics-based estimators can be ascribed to their incompetence at high velocities where the UKF-based estimator has relatively better accuracy. However, the generalisation capability is important as it indicates the applicability in other vehicle models and/or under different test conditions. The dynamics- and kinematics-based estimators are based on physical models, which is convenient for online calibration. Thus, a well-tuned model-based estimator can be easily used in other vehicle models. In contrast, the performance of the NN-based estimator is specific to a certain vehicle model and the test manoeuvres used for model training. Thereby, its generalisation capability is inferior to that of the other estimators (Table 5).

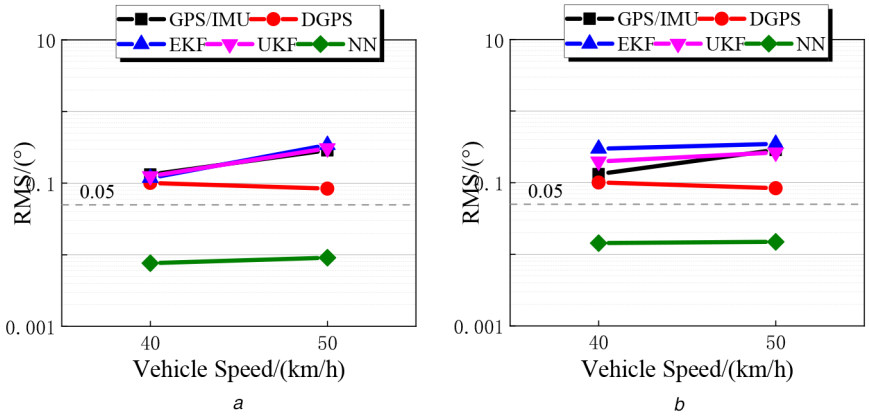

Fig. 18 *Estimation RMSs during the Roundabout network manoeuvre under the road friction coefficient of* ***(a)*** $\mu = 0.6$, ***(b)*** $\mu = 0.9$

Table 5 Performance of each sideslip angle estimator

Estimators	Advantages	Disadvantages	Detail description
GPS-IMU	high velocities	low velocities long-term estimation	low SNR curtails the accuracy at low velocities and error accumulation may fail the estimator
DGPS-IMU	high velocities steering condition	low velocities straight driving long-term estimation	singularity occurs when the yaw rate crosses zeros, which makes it incompetent in the straight-line driving
EKF-/UKF-based	low velocities	high velocities sharp steering	tire model becomes insufficient when the lateral force is large
NN	high and low velocities	system and test condition changes	model accuracy is highly dependent on the training datasets

5 Conclusions

This study presents a comparative study to comprehensively evaluate the performance of the state-of-the-art methods for vehicle sideslip angle estimation under varied velocities and road adhesion conditions. These include kinemics-, dynamics- and NN-based methods. The UKF- and EKF-based estimators are exemplified as the dynamics-based estimators. The advantages and disadvantages of the two dynamics-based estimators are summarised. The results show that they avail only at low vehicle velocities and the UKF has better estimation accuracy to some extent. This may be because the used tire model restricts the applicability of the dynamic-based estimators even the cornering stiffness can be online obtained. Conventional vehicle models may fail to describe vehicle states as encountered during the fishhook manoeuvre. Thus, the dynamics-based estimators are only effective at the velocity range below 50 km/h and with no dramatic steering manoeuvres.

Kinematics-based estimators demonstrate good accuracy especially under large lateral accelerations as shown in the fishhook manoeuvre. Generally, the kinematics-based estimator can still realise sideslip angle estimation at high vehicle velocities and the DGPS-IMU estimator outperforms the GPS-IMU. However, there is significant accumulation error with the increasing implementation time, which makes it suitable for being used in combination of ASSs in short-term employment. In addition, the DGPS-IMU is inapplicable when the vehicle yaw rate is small.

The NN-based estimator yields the best performance in tests. Nevertheless, constructing a complete dataset that can cover all driving conditions is extremely difficult if not impossible. Besides, its applicability in a realistic vehicle controller can be challenging due to intensive computing requirement.

With the development of communication technologies and ITSs, time-consuming computational tasks can be appropriated to a cloud server and the outcomes be sent to vehicle controllers for implementation purpose. This shows the application prospect of NN-based estimators.

6 Acknowledgment

This work was partly supported by the Ministry of Science and Technology of the People's Republic of China (grant number: 2017YFB0103600) and by the Beijing Municipal Science and Technology Commission via the Beijing Nova Program (grant number: Z201100006820007).

7 References

[1] Veres, S.M., Molnar, L., Lincoln, N.K., *et al.*: 'Autonomous vehicle control systems – a review of decision making', *Proc. Instit. Mech. Eng. I-J. Syst. Control Eng.*, 2011, **225**, (I2), pp. 155–195

[2] Cao, J., Liu, H., Li, P., *et al.*: 'State of the art in vehicle active suspension adaptive control systems based on intelligent methodologies', *IEEE Trans. Intell. Transp. Syst.*, 2008, **9**, (3), pp. 392–405

[3] Falcone, P., Borrelli, F., Asgari, J., *et al.*: 'Predictive active steering control for autonomous vehicle systems', *IEEE Trans. Control Syst. Technol.*, 2007, **15**, (3), pp. 566–580

[4] Zhang, H., Wang, J.: 'Active steering actuator fault detection for an automatically-steered electric ground vehicle', *IEEE Trans. Veh. Technol.*, 2017, **66**, (5), pp. 3685–3702

[5] Zhai, L., Sun, T., Wang, J.: 'Electronic stability control based on motor driving and braking torque distribution for a four in-wheel motor drive electric vehicle', *IEEE Trans. Veh. Technol.*, 2016, **65**, (6), pp. 4726–4739

[6] Esmailzadeh, E., Goodarzi, A., Vossoughi, G.R.: 'Optimal yaw moment control law for improved vehicle handling', *Mechatronics*, 2003, **13**, (7), pp. 659–675

[7] Yin, G., Wang, S., Jin, X.: 'Optimal slip ratio based fuzzy control of acceleration slip regulation for four-wheel independent driving electric vehicles', *Math. Probl. Eng.*, 2013, (pt.14), pp. 1–7

[8] Su, W., Rahimi-Eichi, H., Zeng, W., *et al.*: 'A survey on the electrification of transportation in a smart grid environment', *IEEE Trans. Ind. Inf.*, 2012, **8**, (1), pp. 1–10

[9] Hannan, M.A., Azidin, F.A., Mohamed, A.: 'Hybrid electric vehicles and their challenges: a review', *Renew. Sustain. Energy Rev.*, 2014, **29**, pp. 135–150

[10] Shuai, Z., Zhang, H., Wang, J., *et al.*: 'Combined AFS and DYC control of four-wheel-independent-drive electric vehicles over can network with time-varying delays', *IEEE Trans. Veh. Technol.*, 2014, **63**, (2), pp. 591–602

[11] Rajamani, R.: '*Vehicle dynamics and control*' (Springer, USA, 2012, 2nd edn.)

[12] Nam, K., Oh, S., Fujimoto, H., *et al.*: 'Estimation of sideslip and roll angles of electric vehicles using lateral tire force sensors through RLS and Kalman filter approaches', *IEEE Trans. Ind. Electron.*, 2013, **60**, (3), pp. 988–1000

[13] Zhang, H., Wang, J.: 'Vehicle lateral dynamics control through AFS/DYC and robust gain-scheduling approach', *IEEE Trans. Veh. Technol.*, 2016, **65**, (1), pp. 489–494

[14] Geng, C., Mostefai, L., Denai, M., *et al.*: 'Direct yaw-moment control of an in-wheel-motored electric vehicle based on body slip angle fuzzy observer', *IEEE Trans. Ind. Electron.*, 2009, **56**, (5), pp. 1411–1419

[15] Bevly, D.M.: 'Global positioning system (GPS): a low-cost velocity sensor for correcting inertial sensor errors on ground vehicles', *J. Dyn. Syst. Meas. Control-Trans. Asme*, 2004, **126**, (2), pp. 255–264

[16] Chindamo, D., Lenzo, B., Gadola, M.: 'On the vehicle sideslip angle estimation: a literature review of methods, models, and innovations', *Appl. Sci. Basel*, 2018, **8**, (3), p. 355

[17] Chen, B.C., Hsieh, F.C.: 'Sideslip angle estimation using extended Kalman filter', *Veh. Syst. Dyn.*, 2008, **46**, pp. 353–364

[18] Baffet, G., Charara, A., Lechner, D.: 'Estimation of vehicle sideslip, tire force and wheel cornering stiffness', *Control Eng. Pract.*, 2009, **17**, (11), pp. 1255–1264

[19] Melzi, S., Sabbioni, E.: 'On the vehicle sideslip angle estimation through neural networks: numerical and experimental results', *Mech. Syst. Signal Process.*, 2011, **25**, (6), pp. 2005–2019

[20] Vargas-Melendez, L., Boada, B.L., Boada, M.J.L*., et al.*: 'A sensor fusion method based on an integrated neural network and Kalman filter for vehicle roll angle estimation', *Sensors*, 2016, **16**, (9), p. 1400

[21] Zhang, J., Wang, F.-Y., Wang, K*., et al.*: 'Data-driven intelligent transportation systems: a survey', *IEEE Trans. Intell. Transp. Syst.*, 2011, **12**, (4), pp. 1624–1639

[22] Li, S.E., Zheng, Y., Li, K*., et al.*: 'Dynamical modeling and distributed control of connected and automated vehicles: challenges and opportunities', *IEEE Intell. Transp. Syst. Mag.*, 2017, **9**, (3), pp. 46–58

[23] Molina-Masegosa, R., Gozalvez, J.: 'Lte-V for sidelink 5g V2x vehicular communications a new 5g technology for short-range vehicle-to-everything communications', *IEEE Veh. Technol. Mag.*, 2017, **12**, (4), pp. 30–39

[24] Leung, K.T., Whidborne, J.F., Purdy, D*., et al.*: 'A review of ground vehicle dynamic state estimations utilising Gps/Ins', *Veh. Syst. Dyn.*, 2011, **49**, (1–2), pp. 29–58

[25] Guo, H., Cao, D., Chen, H*., et al.*: 'Vehicle dynamic state estimation: state of the art schemes and perspectives', *IEEE-Caa J. Autom. Sinica*, 2018, **5**, (2), pp. 418–431

[26] Jin, X., Yin, G., Chen, N.: 'Advanced estimation techniques for vehicle system dynamic state: a survey', *Sensors*, 2019, **19**, (19), p. 4289

[27] Singh, K.B., Arat, M.A., Taheri, S.: 'Literature review and fundamental approaches for vehicle and tire state estimation*', *Veh. Syst. Dyn.*, 2019, **57**, (11), pp. 1643–1665

[28] Guo, H., Chen, H., Cao, D*., et al.*: 'Design of a reduced-order non-linear observer for vehicle velocities estimation', *IET Control Theory Appl.*, 2013, **7**, (17), pp. 2056–2068

[29] Kim, H.H., Ryu, J.: 'Sideslip angle estimation considering short-duration longitudinal velocity variation', *Int. J. Autom. Technol.*, 2011, **12**, (4), pp. 545–553

[30] Farrelly, J., Wellstead, P.: 'Estimation of vehicle lateral velocity'. Proc. of the 1996 IEEE Int. Conf. on Control Applications held together with IEEE Int. Symp. on Intelligent Control IEEE Int. Symp. on Computer-Aided Control System Design, Dearborn, MI, USA, 15–18 September 1996

[31] Bevly, D.A., Ryu, J., Gerdes, J.C.: 'Integrating Ins sensors with Gps measurements for continuous estimation of vehicle sideslip, roll, and tire cornering stiffness', *IEEE Trans. Intell. Transp. Syst.*, 2006, **7**, (4), pp. 483–493

[32] Rigelsford, J.: 'Automotive control systems: for engine, driveline and vehicle', *Sens. Rev.*, 2004, **24**, (4), pp. 395–395

[33] Selmanaj, D., Corno, M., Panzani, G*., et al.*: 'Robust vehicle sideslip estimation based on kinematic considerations', *IFAC Papers online*, 2017, **50**, (1), pp. 14855–14860

[34] Selmanaj, D., Corno, M., Panzani, G*., et al.*: 'Vehicle sideslip estimation: a kinematic based approach', *Control Eng. Pract.*, 2017, **67**, pp. 1–12

[35] Leung, K.T., Whidborne, J.F., Purdy, D*., et al.*: 'Road vehicle state estimation using low-cost Gps/Ins', *Mech. Syst. Signal Process.*, 2011, **25**, (6), pp. 1988–2004

[36] Bevly, D.M., Sheridan, R., Gerdes, J.C.: 'Integrating Ins sensors with Gps velocity measurements for continuous estimation of vehicle sideslip and tire cornering stiffness'. Proc. of the 2001 American Control Conf., Arlington, VA, USA, 2001, vol. 1–6

[37] Bevly, D.M., Gerdes, J.C., Wilson, C.: 'The use of Gps based velocity measurements for measurement of sideslip and wheel slip', *Veh. Syst. Dyn.*, 2002, **38**, (2), pp. 127–147

[38] Guo, J., Luo, Y., Li, K*., et al.*: 'Coordinated path-following and direct yaw-moment control of autonomous electric vehicles with sideslip angle estimation', *Mech. Syst. Signal Process.*, 2018, **105**, pp. 183–199

[39] Yoon, J.-H., Peng, H.: 'Robust vehicle sideslip angle estimation through a disturbance rejection filter that integrates a magnetometer with Gps', *IEEE Trans. Intell. Transp. Syst.*, 2014, **15**, (1), pp. 191–204

[40] Yoon, J.H., Li, S.E., Ahn, C.: 'Estimation of vehicle sideslip angle and tire-road friction coefficient based on magnetometer with Gps', *Int. J. Autom. Technol.*, 2016, **17**, (3), pp. 427–435

[41] Yoon, J.-H., Peng, H.: 'A cost-effective sideslip estimation method using velocity measurements from two Gps receivers', *IEEE Trans. Veh. Technol.*, 2014, **63**, (6), pp. 2589–2599

[42] Stéphant, J., Charara, A., Meizel, D.: 'Vehicle sideslip angle observers'. 2003 European Control Conf. (ECC), Cambridge, UK, 2003

[43] Doumiati, M., Victorino, A., Charara, A*., et al.*: 'A method to estimate the lateral tire force and the sideslip angle of a vehicle: experimental validation'. 2010 American Control Conf., Baltimore, Maryland, USA, 2010

[44] Nam, K., Fujimoto, H., Hori, Y.: 'Lateral stability control of in-wheel-motor-driven electric vehicles based on sideslip angle estimation using lateral tire force sensors', *IEEE Trans. Veh. Technol.*, 2012, **61**, (5), pp. 1972–1985

[45] Stephant, J., Charara, A., Meizel, D.: 'Virtual sensor: application to vehicle sideslip angle and transversal forces', *IEEE Trans. Ind. Electron.*, 2004, **51**, (2), pp. 278–289

[46] Gadola, M., Chindamo, D., Romano, M*., et al.*: 'Development and validation of a Kalman filter-based model for vehicle slip angle estimation', *Veh. Syst. Dyn.*, 2014, **52**, (1), pp. 68–84

[47] Cheli, F., Ivone, D., Sabbioni, E.: 'Smart tyre induced benefits in sideslip angle and friction coefficient estimation', in Sit, E.W. (ed.): '*Sensors and instrumentation*' (Springer, Switzerland, 2015), vol. **5**, pp. 73–83

[48] Jin, X., Yin, G.: 'Estimation of lateral tire-road forces and sideslip angle for electric vehicles using interacting multiple model filter approach', *J. Franklin Instit. Eng. Appl. Math.*, 2015, **352**, (2), pp. 686–707

[49] Li, L., Jia, G., Ran, X*., et al.*: 'A variable structure extended Kalman filter for vehicle sideslip angle estimation on a low friction road', *Veh. Syst. Dyn.*, 2014, **52**, (2), pp. 280–308

[50] Li, X., Song, X., Chan, C.: 'Reliable vehicle sideslip angle fusion estimation using low-cost sensors', *Measurement*, 2014, **51**, pp. 241–258

[51] Ahangarnejad, A.H., Baslamisli, S.C.: 'Adap-tyre: DEKF filtering for vehicle state estimation based on tyre parameter adaptation', *Int. J. Veh. Des.*, 2016, **71**, (1–4), pp. 52–74

[52] Lian, Y.F., Zhao, Y., Hu, L.L*., et al.*: 'Cornering stiffness and sideslip angle estimation based on simplified lateral dynamic models for four-in-wheel-motor-driven electric vehicles with lateral tire force information', *Int. J. Autom. Technol.*, 2015, **16**, (4), pp. 669–683

[53] Bechtoff, J., Koenig, L., Isermann, R.: 'Cornering stiffness and sideslip angle estimation for integrated vehicle dynamics control', *IFAC Papers online*, 2016, **49**, (11), pp. 297–304

[54] Li, X., Chan, C.-Y., Wang, Y.: 'A reliable fusion methodology for simultaneous estimation of vehicle sideslip and yaw angles', *IEEE Trans. Veh. Technol.*, 2016, **65**, (6), pp. 4440–4458

[55] Morrison, G., Cebon, D.: 'Sideslip estimation for articulated heavy vehicles at the limits of adhesion', *Veh. Syst. Dyn.*, 2016, **54**, (11), pp. 1601–1628

[56] Chen, T., Chen, L., Xu, X*., et al.*: 'Estimation of longitudinal force and sideslip angle for intelligent four-wheel independent drive electric vehicles by observer iteration and information fusion', *Sensors*, 2018, **18**, (4), p. 1268

[57] Liao, Y.-W., Borrelli, F.: 'An adaptive approach to real-time estimation of vehicle sideslip, road bank angles, and sensor bias', *IEEE Trans. Veh. Technol.*, 2019, **68**, (8), pp. 7443–7454

[58] Ma, B., Liu, Y., Gao, Y*., et al.*: 'Estimation of vehicle sideslip angle based on steering torque', *Int. J. Adv. Manuf. Technol.*, 2018, **94**, (9–12), pp. 3229–3237

[59] Doumiati, M., Victorino, A., Charara, A*., et al.*: 'Unscented Kalman filter for real-time vehicle lateral tire forces and sideslip angle estimation'. 2009 IEEE Intelligent Vehicles Symp., Xi'an, People's Republic of China, 2009, vol. 1 and 2

[60] Doumiati, M., Victorino, A.C., Charara, A*., et al.*: 'Onboard real-time estimation of vehicle lateral tire-road forces and sideslip angle', *IEEE-ASME Trans. Mechatron.*, 2011, **16**, (4), pp. 601–614

[61] Chen, J., Sun, X., Chen, L*., et al.*: 'Estimation of vehicle sideslip angle using strong tracking srukf'. Int. Conf. Machinery, Electronics and Control Simulation, Jinzhou, People's Republic of China, 2014

[62] Jia, G., Li, L., Cao, D.: 'Model-based estimation for vehicle dynamics states at the limit handling', *J. Dyn. Syst. Meas. Control-Trans. ASME*, 2015, **137**, (10), pp. 1–8

[63] Singh, K.B.: 'Vehicle sideslip angle estimation based on tire model adaptation', *Electronics*, 2019, **8**, (2), p. 199

[64] Strano, S., Terzo, M.: 'Constrained nonlinear filter for vehicle sideslip angle estimation with no a priori knowledge of tyre characteristics', *Control Eng. Pract.*, 2018, **71**, pp. 10–17

[65] Stephant, J., Charara, A., Meizel, D.: 'Evaluation of a sliding mode observer for vehicle sideslip angle', *Control Eng. Pract.*, 2007, **15**, (7), pp. 803–812

[66] Chen, Y., Ji, Y., Guo, K.: 'A reduced-order nonlinear sliding mode observer for vehicle slip angle and tyre forces', *Veh. Syst. Dyn.*, 2014, **52**, (12), pp. 1716–1728

[67] Grip, H.F., Imsland, L., Johansen, T.A*., et al.*: 'Nonlinear vehicle side-slip estimation with friction adaptation', *Automatica*, 2008, **44**, (3), pp. 611–622

[68] Ding, N., Chen, W., Zhang, Y*., et al.*: 'An extended luenberger observer for estimation of vehicle sideslip angle and road friction', *Int. J. Veh. Des.*, 2014, **66**, (4), pp. 385–414

[69] Gao, X., Yu, Z., Neubeck, J*., et al.*: 'Sideslip angle estimation based on input-output linearisation with tire-road friction adaptation', *Veh. Syst. Dyn.*, 2010, **48**, (2), pp. 217–234

[70] Ma, Y., Guo, H., Wang, F*., et al.*: 'An modular sideslip angle and road grade estimation scheme for four-wheel drive vehicles'. Proc. of the 35th Chinese Control Conf. 2016, Danyang, People's Republic of China, 2016

[71] Zhang, B., Du, H., Lam, J*., et al.*: 'A novel observer design for simultaneous estimation of vehicle steering angle and sideslip angle', *IEEE Trans. Ind. Electron.*, 2016, **63**, (7), pp. 4357–4366

[72] Zhang, H., Huang, X., Wang, J*., et al.*: 'Robust energy-to-peak sideslip angle estimation with applications to ground vehicles', *Mechatronics*, 2015, **30**, pp. 338–347

[73] Zhang, H., Zhang, G., Wang, J.: 'Sideslip angle estimation of an electric ground vehicle via finite-frequency h-infinity approach', *IEEE Trans. Transp. Electrification*, 2016, **2**, (2), pp. 200–209

[74] Chen, T., Chen, L., Cai, Y*., et al.*: 'Robust sideslip angle observer with regional stability constraint for an uncertain singular intelligent vehicle system', *IET Control Theory Appl.*, 2018, **12**, (13), pp. 1802–1811

[75] Chen, T., Chen, L., Xu, X*., et al.*: 'Reliable sideslip angle estimation of four-wheel independent drive electric vehicle by information iteration and fusion', *Math. Probl. Eng.*, 2018, (pt. 4), 1–14

[76] Chen, W., Tan, D., Zhao, L.: 'Vehicle sideslip angle and road friction estimation using online gradient descent algorithm', *IEEE Trans. Veh. Technol.*, 2018, **67**, (12), pp. 11475–11485

[77] Strano, S., Terzo, M.: 'Vehicle sideslip angle estimation via a riccati equation based nonlinear filter', *Meccanica.*, 2017, **52**, (15), pp. 3513–3529

[78] Sakthivel, R., Mohanapriya, S., Kaviarasan, B., *et al.*: 'Non-fragile control design and state estimation for vehicle dynamics subject to input delay and actuator faults', *IET Control Theory Appl.*, 2020, **14**, (1), pp. 134–144
[79] Solmaz, S., Baslamisli, S.C.: 'Simultaneous estimation of road friction and sideslip angle based on switched multiple non-linear observers', *IET Control Theory Appl.*, 2012, **6**, (14), pp. 2235–2247
[80] Fukada, Y.: 'Slip-angle estimation for vehicle stability control', *Veh. Syst. Dyn.*, 1999, **32**, (4–5), pp. 375–388
[81] Cheli, F., Sabbioni, E., Pesce, M., *et al.*: 'A methodology for vehicle sideslip angle identification: comparison with experimental data', *Veh. Syst. Dyn.*, 2007, **45**, (6), pp. 549–563
[82] You, S.-H., Hahn, J.-O., Lee, H.: 'New adaptive approaches to real-time estimation of vehicle sideslip angle', *Control Eng. Pract.*, 2009, **17**, (12), pp. 1367–1379
[83] Zhang, H., Zhang, X., Wang, J.: 'Robust gain-scheduling energy-to-peak control of vehicle lateral dynamics stabilisation', *Veh. Syst. Dyn.*, 2014, **52**, (3), pp. 309–340
[84] Li, J., Zhang, J.: 'Vehicle sideslip angle estimation based on hybrid Kalman filter', *Math. Probl. Eng.*, 2016, pp. 1–10
[85] Madhusudhanan, A.K., Corno, M., Holweg, E.: 'Vehicle sideslip estimation using tyre force measurements'. 2015 23rd Mediterranean Conf. on Control and Automation, Torremolinos, Spain, 2015
[86] Madhusudhanan, A.K., Corno, M., Holweg, E.: 'Vehicle sideslip estimator using load sensing bearings', *Control Eng. Pract.*, 2016, **54**, pp. 46–57
[87] Tanelli, M., Piroddi, L., Savaresi, S.M.: 'Real-time identification of tire-road friction conditions', *IET Control Theory Appl.*, 2009, **3**, (7), pp. 891–906
[88] Kato, M., Isoda, K., Yuasa, H.: 'Estimation of vehicle side slip angle with artificial neural network', *JSAE Rev.*, 1994, **15**, (1), pp. 79–81
[89] Hideaki Sasaki, T.N.: 'A side-slip angle estimation using neural network for a wheeled vehicle'. SAE 2000 World Congress, Detroit, USA, 2000
[90] Du, X., Sun, H., Qian, K., *et al.*: 'A prediction model for vehicle sideslip angle based on neural network', 2010
[91] Chindamo, D., Gadola, M.: 'Estimation of vehicle side-slip angle using an artificial neural network'. 2nd Int. Conf. on Mechanical, Aeronautical and Automotive Engineering, Dalian, People's Republic of China, 2018
[92] Torben Gräber, S.L., Unterreiner, M., Schramm, D.: 'A hybrid approach to side-slip angle estimation with recurrent neural networks and kinematic vehicle models', *IEEE Trans. Intell. Veh.*, 2019, **2018**, pp. 39–47
[93] Miao, P., Liu, G., Zhang, D., *et al.*: 'Sideslip angle soft-sensor based on neural network left inversion for multi-wheel independently driven electric vehicles'. Proc. of the 2014 Int. Joint Conf. on Neural Networks, Beijing, People's Republic of China, 2014
[94] Melzi, S., Resta, F., Sabbioni, E.: 'Vehicle sideslip angle estimation through neural networks: application to numerical data', 2006
[95] De Martino, M., Farroni, F., Pasquino, N., *et al.*: 'Real-time estimation of the vehicle sideslip angle through regression based on principal component analysis and neural networks', 2017 IEEE Int. Systems Engineering Symp., Vienna, Austria, 2017
[96] Bonfitto, A., Feraco, S., Tonoli, A., *et al.*: 'Combined regression and classification artificial neural networks for sideslip angle estimation and road condition identification', *Veh. Syst. Dyn.*, 2019, (4), pp. 1–22
[97] Boada, B.L., Boada, M.J.L., Gauchia, A., *et al.*: 'Sideslip angle estimator based on anfis for vehicle handling and stability', *J. Mech. Sci. Technol.*, 2015, **29**, (4), pp. 1473–1481
[98] Boada, B.L., Boada, M.J.L., Diaz, V.: 'Vehicle sideslip angle measurement based on sensor data fusion using an integrated anfis and an unscented Kalman filter algorithm', *Mech. Syst. Signal Process.*, 2016, **72–73**, pp. 832–845
[99] Novi, T., Capitani, R., Annicchiarico, C.: 'An integrated artificial neural network-unscented Kalman filter vehicle sideslip angle estimation based on inertial measurement unit measurements', *Proc. Instit. Mech. Eng. D-J. Autom. Eng.*, 2019, **233**, (7), pp. 1864–1878
[100] Chen, J., Song, J., Li, L., *et al.*: 'Ukf-based adaptive variable structure observer for vehicle sideslip with dynamic correction', *IET Control Theory Appl.*, 2016, **10**, (14), pp. 1641–1652
[101] Liu, J., Wang, Z., Zhang, L.: 'A time-delay neural network of sideslip angle estimation for in-wheel motor drive electric vehicles'. 2020 IEEE 91st Vehicular Technology Conf. (VTC2020-Spring), Antwerp, Belgium, 2020
[102] Abdul Amir, H.F., Chindamo, D., Gadola, M., *et al.*: 'Estimation of vehicle side-slip angle using an artificial neural network'. MATEC Web of Conf., Singapore, 2018